NANO LETTERS

Letter

pubs.acs.org/NanoLett

Solution-Derived ZnO Homojunction Nanowire Films on Wearable Substrates for Energy Conversion and Self-Powered Gesture Recognition

Ken C. Pradel,[†,∥] Wenzhuo Wu,[†,∥] Yong Ding,[†] and Zhong Lin Wang*[,†,‡,§]

[†]School of Materials Science and Engineering, Georgia Institute of Technology, Atlanta, Georgia 30332-0245, United States

[‡]Beijing Institute of Nanoenergy and Nanosystems, Chinese Academy of Sciences, Beijing, China

[§]Satellites Research Lab., MANA, WPI, National Institute For Materials Science, Tsukuba, Japan

Supporting Information

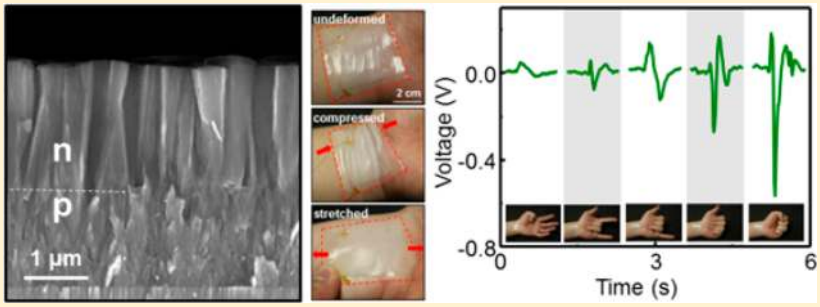

ABSTRACT: Emerging applications in wearable technology, pervasive computing, human−machine interfacing, and implantable biomedical devices demand an appropriate power source that can sustainably operate for extended periods of time with minimal intervention (Wang, Z. L.; et al. *Angew. Chem., Int. Ed.* **2012**, *51*, 11700). Self-powered nanosystems, which harvest operating energy from its host (i.e., the human body), may be feasible due to their extremely low power consumption (Tian, B. Z.; et al. *Nature* **2007**, *449*, 885. Javey, A.; et al. *Nature* **2003**, *424*, 654. Cui, Y.; et al. *Science* **2001**, *291*, 851). Here we report materials and designs for wearable-on-skin piezoelectric devices based on ultrathin (2 μm) solution-derived ZnO p−n homojunction films for the first time. The depletion region formed at the p−n homojunction effectively reduces internal screening of strain-induced polarization charges by free carriers in both n-ZnO and Sb-doped p-ZnO, resulting in significantly enhanced piezoelectric output compared to a single layer device. The p−n structure can be further grown on polymeric substrates conformable to a human wrist and used to convert movement of the flexor tendons into distinguishable electrical signals for gesture recognition. The ZnO homojunction piezoelectric devices may have applications in powering nanodevices, bioprobes, and self-powered human−machine interfacing.

KEYWORDS: *p-type ZnO nanowires, homojunction, solution growth, energy harvesting, gesture control*

Mechanical stimulation is ubiquitous in the environment, making it a strong candidate for continuously powering nanodevices, especially under circumstances where other energy sources, such as solar or thermal energy, may not be readily available.[5−7] Moreover, direct conversion of mechanical agitation into a functional signal may enable active interaction between electronics and a host (e.g., the human body) for novel applications in human-electronic interfacing, biomedical diagnostics, and wearable technology.[8,9] Under mechanical deformation, materials lacking inversion symmetry or with polarization domains produce polarization charges at surfaces/interfaces, known as the piezoelectric effect. This has been widely used for electromechanical sensing, actuation, and energy harvesting.[5,10,11] Traditionally, $Pb(Zr_xTi_{1-x})O_3$ (PZT) has been the piezoelectric material of choice for energy harvesting due to its high piezoelectric coefficient. However, the brittle nature of PZT and presence of lead raises issues for long-term sustainable operation and hinders its application in wearable/implantable technologies.

Since the concept of the nanogenerator (NG) was first introduced in 2006, zinc oxide (ZnO) nanomaterials have served as the model system for studying and applying mechanical energy harvesting in micro/nanoscale systems, due to its good mechanical flexibility, simultaneous piezoelectric and semiconducting properties, easy and low-temperature fabrication, and biocompatibility.[6,12−14] Electricity generation from mechanical stimuli in piezoelectric NGs results in electrons flowing through an external load, which is driven by strain-induced polarization charges in the material.[6] Over the years, as the understanding of the fundamental principles has

Received: July 30, 2014
Revised: October 28, 2014

dx.doi.org/10.1021/nl5029182 | *Nano Lett.* XXXX, XXX, XXX−XXX

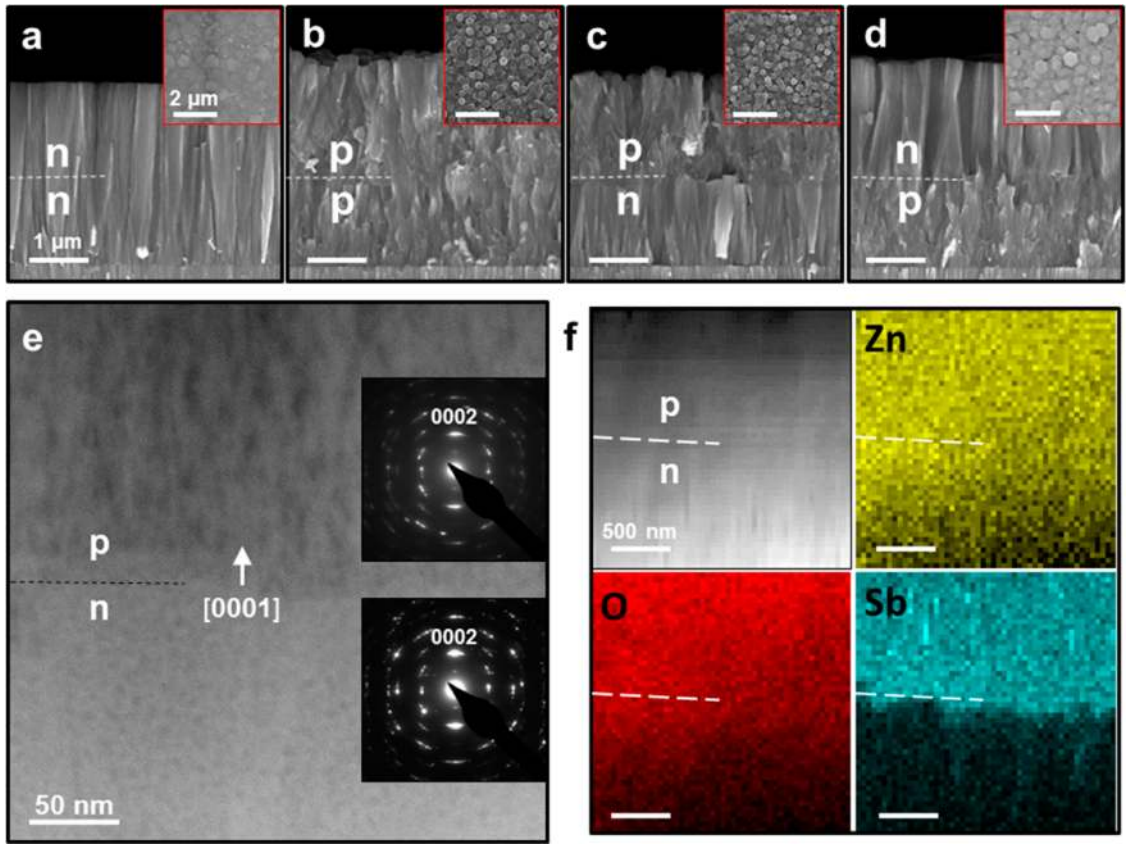

Figure 1. Cross sectional SEM images of multistep ZnO nanowire film growth, in (a) undoped−undoped (nn), (b) 1% doped−1% doped (pp), (c) undoped−1% doped (np), and (d) 1% doped−undoped (pn) configurations. Insets show a top view of the structure. For all images, the naming convention goes from bottom to top. (e) STEM image of the interface between the n-type and p-type nanowires in an **np** structure. The defects in the p-type region are caused by the formation of internal voids during the growth of Sb-doped ZnO. The light pitting observed in undoped region is due to the use of ion milling to thin the sample for analysis. Selected area electron diffraction (SAED) taken from each region shows nearly identical patterns, showing that the *c*-axes for both layers are aligned in the same direction. (f) EDX mapping of the **np** interface showing elemental distribution of Zn, O, and Sb. Lower signal in the bottom region can be attributed to higher sample thickness.

improved, piezoelectric NG technology has advanced significantly, presenting their potential as practical miniaturized power sources.[1] One method to enhance the piezoelectric output in ZnO nanowire NG is through the formation of a p−n junction.[15−17] As ZnO is intrinsically n-type doped, by coating an array of ZnO nanowires (NWs) with a p-type conducting polymer, such as poly(3-hexylthiophene-2,5-diyl) (P3HT), a p−n junction could be formed. Because the polymer attracts free electrons from ZnO, the screening of piezoelectric polarization inside ZnO NWs by free-carriers is reduced, which improves the performance compared to the junction-less device.

Although considerable enhancement has been achieved in these p−n heterojunction devices, it would be advantageous to use p-type ZnO instead to form a homojunction due to the improved chemical stability and mechanical durability between the two ZnO layers. Moreover, the matched band alignment and semiconductor properties between the single-crystalline p-ZnO and n-ZnO NWs may enable interesting applications in functional electronics and optoelectronics. Nevertheless, p-type ZnO has remained a controversial material for many years due to its poor stability. Numerous growth methods incorporating different kinds of dopants have been investigated with varying levels of success.[18−22] Specifically, for NG purposes, solution based hydrothermal method would be ideal, as it operates at relatively low temperatures (<100 °C), allowing for growth on a plethora of substrates including polymers and biodegradable materials. While phosphorus has been used to produce hydrothermally grown ZnO homojunctions,[23,24] their piezoelectric properties have not been investigated. The p-type dopant with the highest recorded stability is antimony, which can also be incorporated through the hydrothermal method and has shown stability of at least 18 months.[25,26] Further work has shown that Sb-doped p-ZnO NW exhibits significant piezoelectric properties by demonstrating its applicability in piezotronic sensing and mechanical energy harvesting.[27]

In this work, ZnO p−n homojunctions were obtained using a hydrothermal method[28] modified with sodium citrate. All chemicals were purchased from Sigma-Aldrich and Alfa Aesar and used as received without further purification. To produce the n-type layers, a solution of 25 mM zinc nitrate, 12.5 mM hexamethylentetramine (HMTA), and 0.7 mM sodium citrate was made in water. Then 0.8 M of ammonium hydroxide was added to the solution to inhibit self-nucleation and precipitation in solution. The substrate was floated face down on the water surface and left to react in an oven at 95 °C for 30 min. To grow p-type ZnO, the precursor concentration and growth time were both doubled in order to compensate for the dopant's interference with normal ZnO growth. A doping level of 1% Sb relative to Zn was chosen, and 0.5 mM of Sb glycolate dopant was added to the solution. The preparation of the doping solution is explained in previous literature.[25] The same

dx.doi.org/10.1021/nl5029182 | *Nano Lett.* XXXX, XXX, XXX−XXX

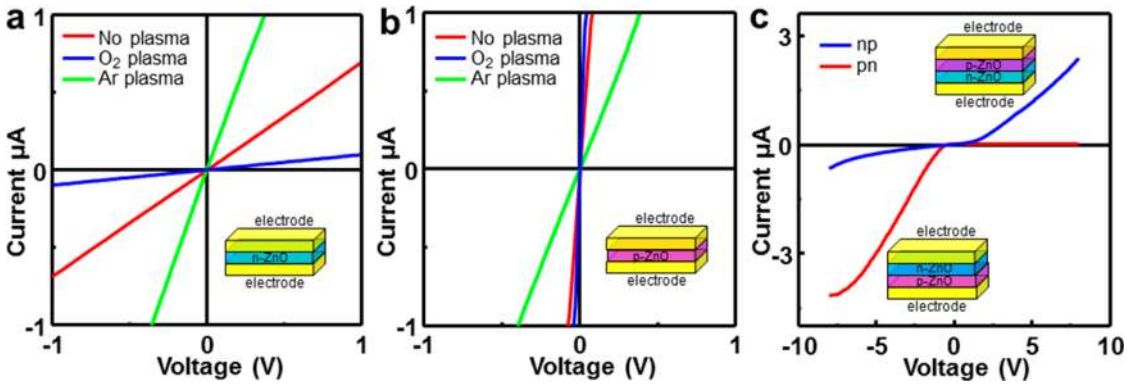

Figure 2. *I*−*V* measurement of (a) n- and (b) p-type films before and after treatment with O_2 or Ar plasma. Opposite trends are observed for each film, with the n-type sample becoming less resistive with Ar plasma treatment, while the p-type one becomes more resistive with the same treatment. The opposite behavior is observed when O_2 plasma is used, as the n-type film becomes more resistive, and the p-type less so. (c) *I*−*V* measurements of the homojunction device grown in both **np** and **pn** configuration. The devices were both subjected to positive bias from the top electrode and show opposite rectification behavior.

amount of ammonium hydroxide was added to this solution. As citrate ions binds preferentially to the (0001) surface of ZnO, growth in the axial direction is inhibited, thus promoting radial growth[29] and causing the NWs to expand and finally coalesce into a densely packed nanowire-film (Figure 1). To prepare the multilayer films, the substrate was put into a fresh solution for continued growth after growing the first layer. As such, we were able to grow both homogeneous and heterogeneous structures (Figure 1a−d) with a controllable thickness of ∼1.5 μm per layer. Samples will be referred to in the order in which the layers were grown, i.e., **np** indicates the first layer grown is undoped (n-type) and the second one grown is p-type doped. From the cross sectional view, the undoped **nn** sample (Figure 1a) has a smooth and continuous growth with an even top surface. However, the growth for **pp** sample (Figure 1b) is much less uniform due to the incorporation of the Sb dopant, producing variation in wire length of about 100 nm, which translates to surface roughness (inset in Figure 1b). In the **np** and **pn** films (Figure 1c,d), we can clearly see the differences in morphology of the doped and undoped films and a clean interface showing where one growth stopped and the other started. The top view of the **np** film (Figure 1c) shows a surface roughness comparable with the **pp** sample. From the top view of the **pn** film (Figure 1d), we can see that the top surface is not as uniform as its **nn** counterpart. The roughness from the underlying p-type layer translated to the n-type growth, producing the observed roughness. The modified hydrothermal method presented here is versatile and stable enough that we can also obtain multilayer samples with alternating layers of doped and undoped films (Figure S1, Supporting Information), making solution-derived ZnO multijunction structures possible for flexible electronics and optoelectronics.[30]

To verify the incorporation of Sb dopant into the films, a cross-section of the **np** sample was analyzed using scanning transmission electron microscopy (STEM). At the interface (Figure 1e), we observed a clear difference in microstructure between the undoped and doped regions. In the doped region, we can see dark voids formed due to the incorporation of Sb atoms during growth, as demonstrated in previous studies.[26,27] When Sb is incorporated into the ZnO lattice during growth, it forms atomic planes perpendicular to the growth direction that interfere with ZnO NW growth. Because of this, ZnO continues to grow around the dopant, forming the observed voids in the NWs. However, the undoped region at the bottom is brighter and more uniform due to the absence of internal defects. The light pitting observed in undoped region is due to the use of ion milling to thin the sample for analysis. Selected area electron diffraction (SAED) patterns were taken from each region, and both had nearly identical patterns, showing that the *c*-axes for both layers are aligned in the same direction (Figure 1e). To further verify the presence of Sb, energy-dispersive X-ray (EDX) mapping was performed at the interface between the two layers (Figure 1f). The Zn and O signals are uniformly distributed throughout the scanned region. The slightly lower signal in the bottom right is due to differences in sample thickness. A significantly stronger Sb signal is observed in the top half of the image, showing that the dopant was only present in the doped region. From the quantitative analysis through an EDX point scan taken on the p-type region (Figure S2, Supporting Information), it was determined that the atomic percentage of Sb was 1.5% (Table S1, Supporting Information), despite the concentration of dopant added to the solution was only 1%. This may be understood as follows. When Sb ions incorporate into the ZnO during NW growth, they cluster together into single-atomic planes.[26] Because subsequent layers of Zn and O cannot attach themselves to the Sb plane, growth simply continues around it, producing the aforementioned voids. Because of the addition of citrate, the growth rate of ZnO in the axial direction slows down, so there is more time for Sb to incorporate itself into the NWs. Additionally, there is always material consumed because of homogeneous nucleation in solution, so not all of the Zn source added to the solution could be incorporated into the as-synthesized sample itself, which may also explain this discrepancy in concentration.

Electrical measurements were performed to further verify the formation of p−n junction through the above process. A transparent conducting oxide (aluminum doped zinc oxide (AZO)) was chosen as electrode material to form both top and bottom electrical contacts with as-synthesized films in all samples. Electrical measurements were performed on a Keithley 4200 semiconductor parameter analyzer. From the two-terminal *I*−*V* measurements, clear linear behaviors are observed for both doped and undoped NW samples, suggesting that AZO forms good Ohmic contacts with both n- and p-ZnO NWs (Figure 2a,b). **pn** and **np** films were grown and measured in a similar fashion. When performing all measurements, the top layer was under positive bias for consistency. Strong rectification behavior is observed for both the **np** and **pn**

dx.doi.org/10.1021/nl5029182 | *Nano Lett.* XXXX, XXX, XXX−XXX

samples, with a turn-on voltage of about 1 V for **np** sample and negative turn-on voltage of −0.5 V for **pn** sample (Figure 2c). A slightly higher leakage current is observed for the **np** sample compared to the **pn** one. Because the p-type wires naturally grow less evenly, the top surface of the **np** sample will be rougher, compared to the **pn** sample (Figure 1c,d). This can lead to a poorer electrical contact in the **np** sample and thus a higher leakage current. These results confirm the successful formation of p−n homojunction regardless of the order in which the n- or p-layers were grown first.

We also investigated the effect of plasma treatment on the transport behavior of these samples. Plasma treatment was performed in a Plasma-Therm reactive ion etcher. For O_2 plasma, a pressure of 300 mTorr, flow rate of 20 sccm, RF power of 200 W, and time of 20 min was used. For Ar plasma treatment, these values were 250 mTorr, 60 sccm, 50 W, and 30 min, respectively. Previous work has shown that treating n-type ZnO with oxygen or argon plasma can modulate its carrier concentration, and thus its piezoelectric properties.[31] As the free charge carriers in the nanowire are primarily responsible for the screening of the piezopotential, a more insulating material should have a stronger piezoelectric output. We first found a baseline resistance of 1.44 MΩ for as-synthesized n-type ZnO. When treated with O_2 plasma, the resistance of n-type ZnO increased to 10.1 MΩ, while it decreased to 0.36 MΩ after treatment with Ar plasma (Figure 2a). These results are consistent with the widely observed dependence of the electrical conductivity of n-type ZnO on the oxygen partial pressure. The exact origin of n-type conductivity in ZnO has been the subject of controversy, and various sources such as a metastable oxygen vacancy configuration,[32] oxygen vacancies stabilized with zinc interstitials,[33] and multicoordinated hydrogen[34] have been proposed to contribute to the unintentional n-type conductivity of ZnO. For p-type ZnO, an opposite trend was observed (Figure 2b). Starting from a baseline resistance of 0.07 MΩ for as-synthesized p-ZnO, when treated with O_2 plasma, the resistance decreased to 0.04 MΩ, while it increased to 0.40 MΩ under Ar plasma. This is likely to be due to the formation or removal of compensating donor defects. As with the undoped n-type sample, the above-mentioned donor sources are removed in p-ZnO under O_2 plasma. Rather than making the material more insulating as is in the n-type sample, this makes p-ZnO more conductive since the relative concentration of free holes increases (blue curve in Figure 2b). The same is true for Ar plasma treatment. As more donor sources are produced, the depletion of free holes makes the material more insulating (green curve in Figure 2b). The changes in resistivity are summarized in Table 1.

Table 1. Resistance of Single ZnO Nanowire Films before and after O_2 or Ar Plasma Treatment (MΩ)

	n-type	p-type
No plasma	1.44	0.07
O_2 plasma	10.1	0.03
Ar plasma	0.36	0.40

In order to determine the effect of homojunction on the piezoelectric output, different architectures were grown and the outputs were measured under consistent deformation (Figure S3, Supporting Information). Stacked layers were grown on 2 × 2 cm flexible polyethylene terephthalate (PET) substrates with a commercially deposited layer of indium tin oxide (ITO) (R_S = 60 Ω/sq) as a bottom electrode. The as-grown structure was then spin coated with PMMA A6 at 2000 rpm to form an insulating layer to prevent current leakage. AZO was sputtered on top of the whole structure as the top electrode, and test wires were affixed to the two electrodes using conductive silver paste. Finally, the whole structure was coated with a layer of polydimethylsiloxane (PDMS) as a packaging layer, producing a complete energy harvester. The resulting structure is shown both pictorially and schematically in Figure 3a. Single layers of n- and p-type ZnO were used as the baseline for piezoelectric measurements (Figure 3b,c). In the experiment, compressive strain of −0.22% (calculation shown in Supporting Information) was periodically induced in the NW film by deforming the PET substrate. Since the polar axis (red arrow in Figure 3a)

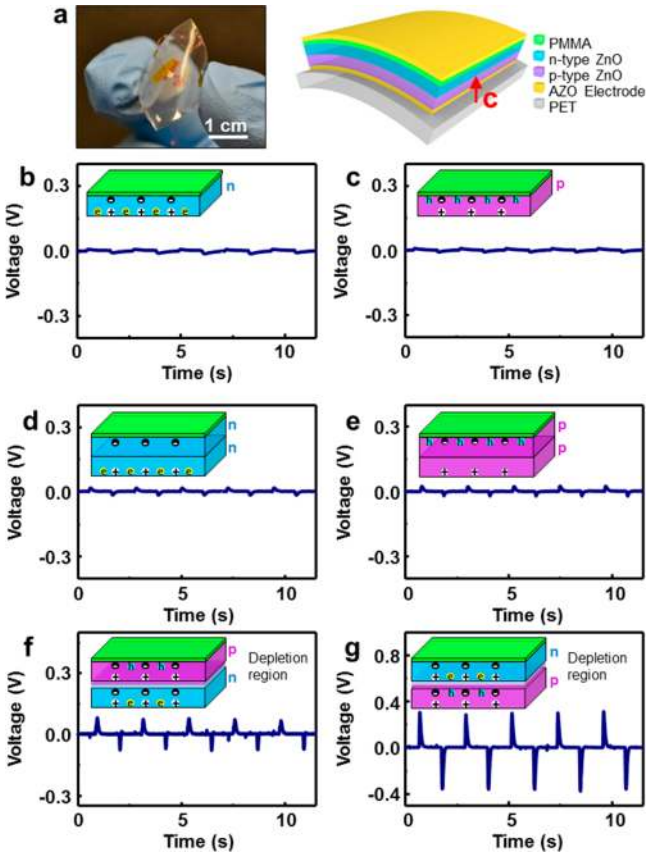

Figure 3. (a) Photograph and schematic of the homojunction nanogenerator. Component thicknesses are exaggerated for clarity. Open circuit voltage output of the nanogenerator under cyclic deformation for (b) n- and (c) p-type nanogenerator. The "+" and "−" in the inset schematics represent the piezopolarization charges in ZnO under compressive strain, while "e" and "h" represent free electrons and holes present in the films. Because the polar axis points away from the substrate, under compressive strain caused by bending, negative/positive polarization charges are induced at the top/bottom of the film. For the stacked homogeneous (d) nn and (e) pp structures, a slightly improved output is observed due to increased sample thickness, which is equivalent to two devices connected in series. The (f) np structure shows a significant improvement as the formation of the depletion region reduces the free charge carrier concentration, thus decreasing the screening effect. The most significant improvement is seen in the (g) pn configuration as in addition to the formation of the depletion region, the free electrons and holes in the n- and p-type layers, respectively, are attracted toward the junction, leaving the piezopolarization charges at the electrodes effectively unscreened.

dx.doi.org/10.1021/nl5029182 | *Nano Lett.* XXXX, XXX, XXX−XXX

points away from the substrate in both the n- and p-ZnO NW films as confirmed in Figure 1b, negative/positive piezoelectric polarization charges ("−" and "+") are induced at the top/bottom of the films under compressive strain. The negative polarization charges can drive electrons through an external circuit to screen the positive polarization charges at the bottom of the film and balance out the difference between quasi-Fermi levels at the top and bottom electrodes. This gives rise to the positive pulse observed in experiment. The response time of these devices can be measured by measuring the time from zero output to the peak. From this, we found a response time of 40 ms (Figure S4, Supporting Information), which is on a similar order of magnitude as previous studies on ZnO nanowires.[35,36] When the strain is released, the piezoelectric polarization disappears, and the electrons that had once screened the positive polarization charges flow back through the external circuit and produce the negative pulse. Both kinds of NW films also experience internal screening of piezoelectric polarization by free carriers. The "e" and "h" symbols represent negative and positive free carriers in n- and p-ZnO, respectively (Figure 3). The average output voltages of the as-synthesized n- and p-type samples were 7.10 and 7.13 mV, respectively (Figure 3b,c).

We then proceeded to measure the piezoelectric output of bilayer structures to see how adding a homojunction changes the output. To start, bilayer structures with single conductivity type was measured, and an average output of 13.9 and 24.2 mV was observed for the **nn** and **pp** structures, respectively (Figure 3d,e). This output makes sense with respect to the single layer samples (Figure 3b,c), as bilayer structures possess twice the thickness of the piezoelectric layers. This is analogous to connecting two single layer devices in series, which in principle doubles the output voltage. When an **np** nanogenerator is made, a noticeably higher output is observed (150 mV) compared to the single component bilayer structure (Figure 3f). Because of the formation of the depletion region, the free charge carrier concentration in each layer is reduced, although there is still some amount of screening. Therefore, we see a significant improvement in the output compared to that of the bilayer structures with single conduction type. For the **pn** structure, the output increased by over an order of magnitude to 284 mV compared to the **nn** and **pp** samples. In this case, the free electrons and holes remaining in the n- and p-type layers after the formation of the depletion region are attracted to the junction area to screen the respective piezopolarization charges (Figure 3g). As a result, the piezocharges at the electrodes are essentially unscreened, leading to a great improvement in the piezoelectric output. The hydrothermal method is naturally prone to some variability in nanowire dimensions and doping which can affect the resulting nanogenerators piezoelectric output. Previous work on p-type ZnO nanowires[27] showed that increasing the doping level reduced the nanogenerator output, due to increased screening, so fluctuations in doping between samples could affect the output. Fluctuations in wire dimensions can also have an effect on output, as the piezopotential is governed by the nanowire aspect ratio.[37] On the basis of the SEM images in Figure 1, we can conclude that nanowire growth within a single sample is not variable enough to warrant concern. Furthermore, by growing new **np** and **pn** samples and repeating nanogenerator measurements (Figure S5, Supporting Information), consistent output was observed. The average peak output from these devices (163 and 306 mV) only differed from those in Figure 3 by less than 10%, showing that devices produced with hydrothermally grown nanowires are reasonably consistent. The corresponding output currents are shown in Figure S6, Supporting Information, and summarized in Table 2, and the same trends are observed as a result of changes in screening. Compared to early studies of piezoelectric nanogenerators[38] with output voltage on the order of 80 mV, the output obtained in the **pn** structure is significantly improved. With optimized design and packaging, ZnO-based nanogenerators with output on the order of tens of volts could be obtained.[39] By comparison, the structure presented in this work is relatively simple in order to emphasize the study of the fundamental materials system.

Table 2. Average Peak Piezoelectric Current Output for Homojunction Structures Not Subject to Plasma Treatment

configuration	voltage (mV)	current (nA)
n	7.10	1.66
p	7.13	0.56
nn	13.9	0.473
pp	24.2	0.246
np	150	0.985
pn	284	10.6

To quantify the power output of the piezoelectric device, it is necessary to study the voltage and current outputs as a function of load resistance, as shown in Figure S7, Supporting Information. The power output of the weakest and strongest devices, **n** and **pn**, were compared. In both cases, the output current is constant for load resistance up to ∼10 MΩ and then falls with increasing load, while the output voltage increases when the resistance exceeds 10 MΩ and tapers off around 2 GΩ. The maximum instantaneous power delivered onto the load for the **n** device of 1.1 pW occurs when load resistance is 110 MΩ, and a largely enhanced power output of 232 pW for **pn** device is achieved when load resistance is 22 MΩ.

We then proceeded to investigate the change in output when the structures described earlier were treated with O_2 or Ar plasma. As demonstrated earlier in Figure 2, with the appropriate plasma treatment, the free charge carrier concentration in both n- and p-ZnO can be reduced, which mitigates the screening of piezoelectric polarization and thus improves the piezoelectric output for the single layer device. Single layer devices were fabricated and treated with the appropriate plasma to increase the output voltage ($\mathbf{n}_{O2}$ and $\mathbf{p}_{Ar}$). The output increased by an order of magnitude when compared to the **n** and **p** samples from Figure 3, to 55.3 and 66.9 mV, for $\mathbf{n}_{O2}$ and $\mathbf{p}_{Ar}$, respectively (Figure 4a,b).

Because the same plasma treatment has opposite effects depending on whether the material is n- or p-type, treating a homojunction structure with the same plasma will make one layer more insulating and thus more piezoelectric, while making the other layer more conductive and less piezoelectric. On this basis we investigated the effect of ZnO p−n homojunction on piezoelectric NG outputs when only one layer in the homojunction structure is piezoelectric, while the other is more conducting. The first group of samples includes the **np** structure (Figure 4c,d). In an O_2 plasma treated **np** structure ($\mathbf{n}_{O2}\mathbf{p}_{O2}$), the bottom n-type layer becomes more insulating and thus more piezoelectric, while the top p-type layer is more conducting, thus making its contribution to output negligible when compared to their as-synthesized counterparts (Figure 4c). Under compressive strain, the positive piezoelectric

dx.doi.org/10.1021/nl5029182 | Nano Lett. XXXX, XXX, XXX−XXX

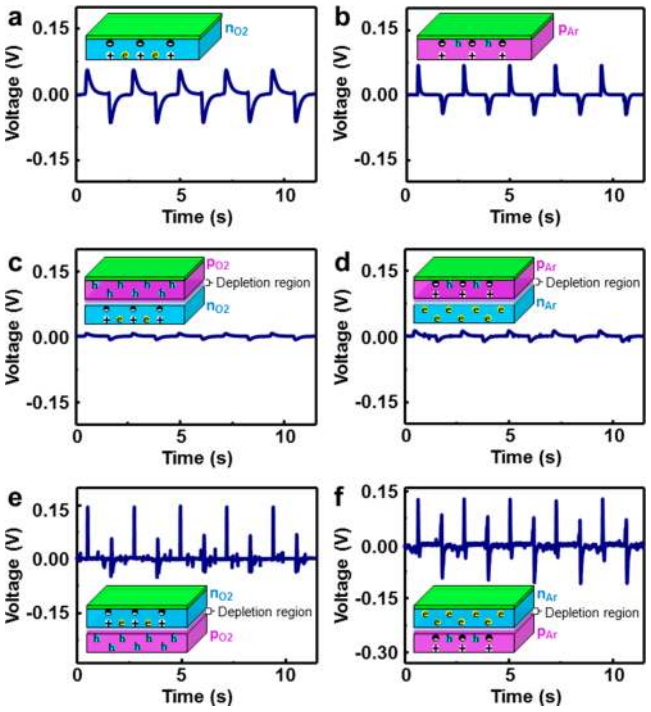

Figure 4. Output voltage for single layer and homojunction structures treated with either O_2 or Ar plasma. The sample naming convention follows that of the main text and the suffix denotes the plasma treatment used. Treating the n-type layer with (a) O_2 plasma ($\mathbf{n_{O2}}$) reduces the free electron concentration, thus improving the output voltage compared to the untreated sample in Figure 3b. A similar trend is observed for (b) the p-type layer when treated with Ar plasma ($\mathbf{p_{Ar}}$) due to the reduction in free hole concentration. When the **np** structure is treated with either (c) O_2 or (d) Ar plasma, the output voltage is greatly reduced compared to the single layer cases. In the **pn** configuration, a noticeable improvement is observed for (e) O_2 and (f) Ar plasma treated samples.

polarization charges in the $\mathbf{n_{O2}}$ layer should experience even less internal screening as there is a lower concentration of free electrons because of the formation of the depletion region. However, the output is only 7 mV, much weaker than the $\mathbf{n_{O2}}$ sample (Figure 4a). This is because the thick conducting $\mathbf{p_{O2}}$ layer is dampening the effect of the negative piezoelectric polarization charges induced near the top surface of the bottom n-type layer. Similarly, for the Ar plasma treated **np** structure ($\mathbf{n_{Ar}p_{Ar}}$), a reduced output (12.2 mV) compared to the $\mathbf{p_{Ar}}$ sample is observed (Figure 4d). Here, the bottom n-type layer is more conducting and the top p-type layer is more piezoelectric than their pristine counterparts. The partial screening in $\mathbf{p_{Ar}}$ layer due to free carriers (holes) is further reduced because of the formation of the depletion region. However, the output is reduced due to the rapid screening of the positive piezoelectric polarization in the $\mathbf{p_{Ar}}$ layer by free electrons from the n-type layer, leading to the significantly lower output observed.

However, when a **pn** structure is used, the output is enhanced relative to the single layer device (Figure 4e,f). In an O_2 plasma treated **pn** structure ($\mathbf{p_{O2}n_{O2}}$) (Figure 4e), the bottom p-layer is conductive while the top n-layer is piezoelectric. Under compressive strain, the positive piezopolarization charges induced at the bottom surface of the top n-layer experience less internal screening from free electrons due to the O_2 plasma treatment and the depletion region formation. Additionally, the junction is now under reverse bias due to the distribution of piezoelectric polarization. It has been previously demonstrated that a p−n junction under reverse bias can function similarly to the Schottky barrier used in typical piezoelectric nanogenerator.[15] As the junction inhibits the flow of electrons from the circuit into the nanomaterials, the screening effect is slowed down. Moreover, the negative piezopolarization charges induced at the top surface of the top n-layer are undampened and can more effectively drive electrons through the top electrode and external circuit, producing enhanced piezoelectric output of 146 mV (Figure 4f). Enhancement is also observed in the Ar plasma treated **pn** structure ($\mathbf{p_{Ar}n_{Ar}}$) sample, where the bottom p-layer is piezoelectric while the top n-layer is conductive. The positive piezopolarization charges induced at the bottom surface of the bottom p-layer is unscreened, while the negative piezopolarization charges experience reduced screening because of both the Ar-plasma treatment and the formation of the depletion region. These negative piezopolarization charges can effectively repel electrons in the n-type region, which accumulate at the interface with the PMMA layer. Both the negative piezocharges and the undampened positive piezocharges in the p-layer drive electrons through the rest of the circuit, producing significant piezoelectric output of 123 mV (Figure 4f). The average outputs obtained are summarized in Table 3 and corresponding output currents in Figure S8, Supporting Information.

Table 3. Average Peak Piezoelectric Current Output for Single Layer and Homojunction Structures under Different Plasma Treatment

	O_2 plasma		Ar plasma	
configuration	voltage (mV)	current (nA)	voltage (mV)	current (nA)
n	55.3	1.17	n/a	n/a
p	n/a	n/a	66.9	1.18
np	7.00	0.269	12.2	0.528
pn	146	3.04	123	3.67

In addition to mechanical energy harvesting, piezoelectric nanodevices may also find unique applications as self-powered active sensors without external bias for detecting small-scale motion in biological systems[7,40] and potentially enabling novel human machine interfacing.[41] In particular, there has been a growing interest in wearable systems for hand gesture recognition for remote sensing and controlling. Visual approaches using cameras and computer vision algorithms have been implemented to interpret sign language with great success[42,43] but require external equipment and adequate lighting to function. The identification and recognition of posture, gait, and human behaviors have also been realized by wearable electronics based on electromyography[44] or photoreflector arrays,[45] but neither device is truly conformable to the human body. Recent progress in skin-like electronics for measuring surface electromyography enables novel human−machine interface conformable to human skin.[46] However, all these existing technologies for gesture recognition require an external power source, which may complicate the system design and limit operation schemes. Inspired by this, we explored the feasibility of our p−n homojunction piezoelectric devices for wearable self-powered gesture recognition, which can directly recognize the small-scale movement of human muscles and convert it into electrical controlling signals without additional power source. As we obtained the maximum output from the

dx.doi.org/10.1021/nl5029182 | *Nano Lett.* XXXX, XXX, XXX−XXX

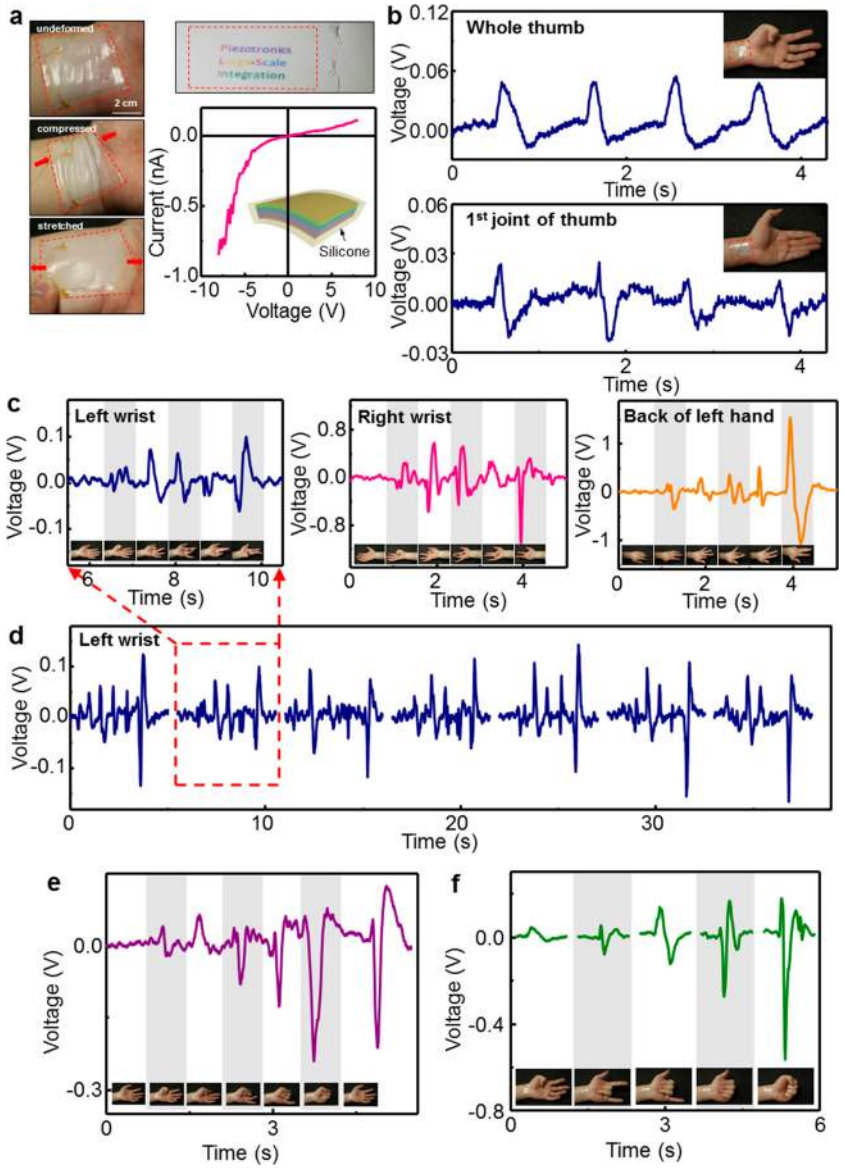

Figure 5. Homojunction nanogenerator grown in the pn configuration on silicone rubber for gesture recognition by measurement of flexor movement. (a) Photographs show the device conformability when mounted on a human wrist (left). The device is also highly transparent (top), as printed text underneath it is still clearly legible. The IV characteristics of the device was measured as before, confirming the presence of a pn junction. (b) The output of the device was measured as a function of the difference in flexion of the thumb. When the whole thumb is bent, a significantly higher output peak is observed, while maintaining a similar signal pattern. (c) The device was used to measure signals when fingers were individually flexed and extended starting with the left wrist. A distinct signal pattern is observed for each finger. The same pattern was repeated with the right hand (center), producing a similar pattern, but with higher intensity. The device was attached to the back of the hand (right) to measure movement of the extensor tendons, producing a unique signal. (d) By repeating the same gesture several times with the left-hand, the device's stability was demonstrated. (e) The fingers were then sequentially bent starting with the thumb, but unlike the previous pattern, were not released until the end, producing unique "half signals" compared to previous gestures. (f) Multifinger gestures were used to demonstrate the device's ability to detect more complex gestures. In order, the patterns are thumb; middle and ring; index, middle, and ring; index, middle, ring, and little; and all five fingers.

pn device, we proceeded to use this architecture to develop an ultrathin, wearable piezoelectric device for detecting movement in flexor muscles in human fingers. A 5 × 5 cm^2 piece of glass was first spin-coated with ~100 nm of PMMA A2 at 1000 rpm for 1 min, followed by a 30 μm layer of Ecoflex at 1000 rpm for 1 min. After curing, AZO was sputtered onto the surface under the same conditions as the previous PET devices, and nanowire films were grown in the **pn** configuration. During growth, a portion of the substrate was covered with PTFE tape in order to prevent growth on the bottom electrode contact. After growth, a 20 μm layer of Ecoflex was spin-coated on at 2000 rpm for 1 min, followed by the AZO top electrode. Wire leads were connected to the two electrodes using silver paste, and the whole device was encapsulated with a 300 μm layer of Ecoflex for protection. Finally, the device was put into acetone to dissolve the underlying PMMA layer and release it from the glass substrate.

The final device has a high degree of transparency and flexibility (Figure 5a). A representative cross-sectional illustration of the structure is shown in Figure S9, Supporting Information, with the neutral strain plane defined by a red dashed line. Since the ZnO homojunction bilayer is below the

dx.doi.org/10.1021/nl5029182 | *Nano Lett.* XXXX, XXX, XXX−XXX

neutral strain plane, both n- and p-layers will experience pure compressive/tensile strains when the entire device is mechanically deformed. The small modulus (~55 kPa[47]) and thickness of the device (~350 μm) allows for good adhesion of the device to the skin by van der Waals forces, without needing hardware fixture or adhesive tapes, and the underlying skin can still naturally stretch and fold with minimal interference (Figure 5a). Transport measurement confirmed the successful formation of a p−n junction in the final device.

To demonstrate a device's applicability, it was attached to a human wrist to detect movement of the underlying tendons, and the piezoelectric output produced based on different hand gestures was measured. We first probed our device's capability of detecting the difference in muscle movement even when the behavior of the same finger varies slightly. First the thumb was quickly bent and extended, producing a 50 mV pulse with each cycle (Figure 5b, top). Furthermore, by repeating the same motion with only the first joint of the thumb, a smaller voltage pulse (15 mV) is produced. As a similar signal pattern is observed, the degree of bending can be identified based on signal intensity. Using this as a starting point, we proceeded to compare output based on individual fingers being bent. In a relaxed state, no output voltage was measured. Each finger was then bent and released in sequence starting with the thumb, producing distinct current pulses (Figure 5c, left). The movement of the fingers is controlled by a variety of muscle groups. The extrinsic muscle group in the forearm, the flexor digitorum superficialis, controls flexion of the index, middle, ring, and little finger, while the thenar muscle group in the hand controls the thumb.[48] Since distinct outputs with characteristic patterns were observed for each finger, it suggests that the flexion of each individual finger can be identified based on the pattern shape from our piezoelectric device. A much larger pulse is observed when the little finger is flexed. This is because a separate group of muscles in the palm, the hypothenar eminence, also controls movement of the little finger. Because of the device's proximity to the palm, movement from both the hypothenar and flexor muscles are detected, thus producing a larger pulse. To show device consistency, the same device was attached to the subject's right-hand wrist, and the same sequence was performed. A similar pattern was observed, albeit with higher signal amplitude (Figure 5c, middle). We believe that this is because the device is attached to the subject's dominant hand, which is naturally stronger and more dexterous. Some similarities are observed between this pattern and those observed in the left hand, most notably that the little finger is still the dominant signal. The device was also attached to the back of the subject's left hand to measure output from the extensor tendons during gesturing. The output voltage was over an order of magnitude greater than those measured from the wrist (Figure 5c, right). As the tendons are much closer to the surface of the skin in this case, we can expect a much stronger signal from this device. The pattern observed in this position differs significantly from the signals from the wrist. By using two or more devices in conjunction with each other, a more complex signal pattern can be obtained allowing for higher resolution gesture recognition with enhanced sensitivity and accuracy. To demonstrate the device stability, the output voltage was measured when the same gesture sequence was repeated for multiple cycles (Figure 5d). Because of the inconsistencies inherent to something as complex as finger motions, only representative output curves are presented here. The original output for these sequences is presented in Figure S10, Supporting Information.

To develop a deeper understanding of this device's operation for gesture detection, the output for different gestures was investigated. The subject's fingers were bent in sequence starting with the thumb. However, in this case, the fingers were only released after all of them had been bent. A different signal pattern is observed for the thumb in this case, as it was kept bent and hence only partial patterns corresponding to the bent state from the signals in Figure 5c was observed. When all five fingers are released, a large pulse is observed with its own distinct signal pattern. A video of the device in action was taken (Supporting Information), and a clear correlation between output signal and which finger was bent can be observed. While the extensors on the opposite side of the wrist control finger movement when they are extended, the movement of these tensors can still be detected by our device as they are relaxed. For our device to be a fully functional gesture detector, the signals when multiple fingers are bent simultaneously must also be distinguished. The bent thumb (1 finger) from earlier measurement was used as a baseline (Figure 5f). Next, the middle and ring fingers were bent and straightened simultaneously (2 fingers), producing a slightly higher peak output with a different shape. The output increases again when the index finger is added (3 fingers); however, the difference in peak output is not equal to that of bending the index finger individually, showing that this is not a simple additive process. Once the little finger is added (4 finger), its output dominates over the others resulting in a much sharper output. Finally, when a clenched fist is formed (5 fingers), the highest output is observed at −0.6 V. The signal shape is similar to that of the 4 finger case, as the little finger is still the dominant signal. Corresponding output currents for these devices are shown in Figure S11, Supporting Information.

In conclusion, we have demonstrated for the first time the applicability of ZnO homojunction nanostructures for enhanced mechanical energy harvesting. By systematically designing and testing different material configurations and treatments, we were able to find the optimum materials design, and the resulting output is in agreement with previous fundamental theories on the working mechanism of piezoelectric NGs. The synthesis method presented in this work for producing densely packed NW films shows that these may serve as viable alternatives to conventional sputtered thin-films owing to their very low synthesis temperature. While this study only focused on bilayer structures, it shows the potential to produce more intricate n−p−n or p−n−p bipolar junctions for more complex electronics. Furthermore, the presented ultrathin wearable piezoelectric device based on ZnO homojunction nanostructures is capable of detecting small-scale subdermal movement from the tendons in the human wrist and distinguishing different motions and hand gestures. The electronic output signals from our devices after processing the encoded information in ambient stimuli such as the muscle movement may make possible the control of embedded electronics and sensors for intelligent and adaptive operations in human−electronics interfacing, bioprobes, and therapeutic devices.

■ ASSOCIATED CONTENT

Supporting Information

SEM images taken of trilayer homojunction structures. EDX point scan taken of the p-type layer. Explanation and schematic

dx.doi.org/10.1021/nl5029182 | Nano Lett. XXXX, XXX, XXX−XXX

of strain applied to the nanogenerators in this letter. Response time measurement for **pn** device and repeat measurements of the **np** and **pn** devices. Current measurements corresponding to the devices tested in Figures 3 and 4 and calculated peak power output under load for the **n** and **pn** devices. Schematic, raw voltage output, and current output of the silicone nanogenerator for different gestures. Video of the silicone nanogenerator detecting individual finger motion. This material is available free of charge via the Internet at http://pubs.acs.org.

AUTHOR INFORMATION

Corresponding Author

*E-mail: zhong.wang@mse.gatech.edu.

Author Contributions

‖These authors contributed equally to this work.

Notes

The authors declare no competing financial interest.

ACKNOWLEDGMENTS

Research was supported by U.S. Department of Energy, Office of Basic Energy Sciences (Award DE-FG02-07ER46394), MANA, National Institute For Materials Science, Japan, a joint project with Sungkyunkwan University, Korea, the Hightower Chair foundation, and the "thousands talents" program for pioneer researcher and his innovation team, China, Beijing City Committee of science and technology (Z131100006013004 and Z131100006013005), and National Natural Science Foundation of China (Grant No. 51432005).

REFERENCES

(1) Wang, Z. L.; Wu, W. Z. *Angew. Chem., Int. Ed.* **2012**, *51*, 11700−11721.

(2) Tian, B. Z.; Zheng, X. L.; Kempa, T. J.; Fang, Y.; Yu, N. F.; Yu, G. H.; Huang, J. L.; Lieber, C. M. *Nature* **2007**, *449*, 885−U8.

(3) Javey, A.; Guo, J.; Wang, Q.; Lundstrom, M.; Dai, H. J. *Nature* **2003**, *424*, 654−657.

(4) Cui, Y.; Lieber, C. M. *Science* **2001**, *291*, 851−853.

(5) Wang, Z. L.; Song, J. H. *Science* **2006**, *312*, 242−246.

(6) Yang, R. S.; Qin, Y.; Dai, L. M.; Wang, Z. L. *Nat. Nanotechnol.* **2009**, *4*, 34−39.

(7) Dagdeviren, C.; Yang, B. D.; Su, Y. W.; Tran, P. L.; Joe, P.; Anderson, E.; Xia, J.; Doraiswamy, V.; Dehdashti, B.; Feng, X.; Lu, B. W.; Poston, R.; Khalpey, Z.; Ghaffari, R.; Huang, Y. G.; Slepian, M. J.; Rogers, J. A. *Proc. Natl. Acad. Sci. U.S.A.* **2014**, *111*, 1927−1932.

(8) Wang, Z. L. *Adv. Mater.* **2012**, *24*, 4632−4646.

(9) Wu, W. Z.; Pan, C. F.; Zhang, Y.; Wen, X. N.; Wang, Z. L. *Nano Today* **2013**, *8*, 619−642.

(10) Ferren, R. A. *Nature* **1991**, *350*, 26−27.

(11) Kingon, A. I.; Srinivasan, S. *Nat. Mater.* **2005**, *4*, 233−237.

(12) Wang, Z. L.; Song, J. *Science* **2006**, *312*, 242−246.

(13) Qin, Y.; Wang, X. D.; Wang, Z. L. *Nature* **2008**, *451*, 809−U5.

(14) Chang, C. E.; Tran, V. H.; Wang, J. B.; Fuh, Y. K.; Lin, L. W. *Nano Lett.* **2010**, *10*, 726−731.

(15) Briscoe, J.; Stewart, M.; Vopson, M.; Cain, M.; Weaver, P. M.; Dunn, S. *Adv. Energy Mater.* **2012**, *2*, 1261−1268.

(16) Lee, K. Y.; Kumar, B.; Seo, J.-S.; Kim, K.-H.; Sohn, J. I.; Cha, S. N.; Choi, D.; Wang, Z. L.; Kim, S.-W. *Nano Lett.* **2012**, *12*, 1959−1964.

(17) Chung, S. Y.; Kim, S.; Lee, J.-H.; Kim, K.; Kim, S.-W.; Kang, C.-Y.; Yoon, S.-J.; Kim, Y. S. *Adv. Mater.* **2012**, *24*, 6022−6027.

(18) Fan, J. C.; Sreekanth, K. M.; Xie, Z.; Chang, S. L.; Rao, K. V. *Prog. Mater. Sci.* **2013**, *58*, 874−985.

(19) Lee, W.; Jeong, M. C.; Myoung, J. M. *Appl. Phys. Lett.* **2004**, *85*, 6167−6169.

(20) Xiang, B.; Wang, P. W.; Zhang, X. Z.; Dayeh, S. A.; Aplin, D. P. R.; Soci, C.; Yu, D. P.; Wang, D. L. *Nano Lett.* **2007**, *7*, 323−328.

(21) Yuan, G. D.; Zhang, W. J.; Jie, J. S.; Fan, X.; Zapien, J. A.; Leung, Y. H.; Luo, L. B.; Wang, P. F.; Lee, C. S.; Lee, S. T. *Nano Lett.* **2008**, *8*, 2591−2597.

(22) Chu, S.; Wang, G. P.; Zhou, W. H.; Lin, Y. Q.; Chernyak, L.; Zhao, J. Z.; Kong, J. Y.; Li, L.; Ren, J. J.; Liu, J. L. *Nat. Nanotechnol.* **2011**, *6*, 506−510.

(23) Fang, X.; Li, J.; Zhao, D.; Shen, D.; Li, B.; Wang, X. *J. Phys. Chem. C* **2009**, *113*, 21208−21212.

(24) Hwang, S.-H.; Moon, K.-J.; Lee, T. I.; Lee, W.; Myoung, J.-M. *Mater. Chem. Phys.* **2014**, *143*, 600−604.

(25) Wang, F.; Seo, J.-H.; Bayerl, D.; Shi, J.; Mi, H.; Ma, Z.; Zhao, D.; Shuai, Y.; Zhou, W.; Wang, X. *Nanotechnology* **2011**, *22*, 225602.

(26) Yankovich, A. B.; Puchala, B.; Wang, F.; Seo, J. H.; Morgan, D.; Wang, X. D.; Ma, Z. Q.; Kvit, A. V.; Voyles, P. M. *Nano Lett.* **2012**, *12*, 1311−1316.

(27) Pradel, K. C.; Wu, W. Z.; Zhou, Y. S.; Wen, X. N.; Ding, Y.; Wang, Z. L. *Nano Lett.* **2013**, *13*, 2647−2653.

(28) Xu, C.; Shin, P.; Cao, L.; Gao, D. *J. Phys. Chem. C* **2009**, *114*, 125−129.

(29) Tian, Z. R.; Voigt, J. A.; Liu, J.; McKenzie, B.; McDermott, M. J.; Rodriguez, M. A.; Konishi, H.; Xu, H. *Nat. Mater.* **2003**, *2*, 821−826.

(30) Wu, W. Z.; Wen, X. N.; Wang, Z. L. *Science* **2013**, *340*, 952−957.

(31) Wu, W.; Wang, Z. L. *Nano Lett.* **2011**, *11*, 2779−2785.

(32) Lany, S.; Zunger, A. *Phys. Rev. B* **2005**, *72*, 035215.

(33) Kim, Y.-S.; Park, C. H. *Phys. Rev. Lett.* **2009**, *102*, 086403.

(34) Janotti, A.; Van de Walle, C. G. *Nat. Mater.* **2007**, *6*, 44−47.

(35) Zhou, J.; Fei, P.; Gao, Y.; Gu, Y.; Liu, J.; Bao, G.; Wang, Z. L. *Nano Lett.* **2008**, *8*, 2725−2730.

(36) Zhou, J.; Gu, Y.; Fei, P.; Mai, W.; Gao, Y.; Yang, R.; Bao, G.; Wang, Z. L. *Nano Lett.* **2008**, *8*, 3035−3040.

(37) Gao, Y.; Wang, Z. L. *Nano Lett.* **2007**, *7*, 2499−2505.

(38) Xu, S.; Qin, Y.; Xu, C.; Wei, Y.; Yang, R.; Wang, Z. L. *Nat. Nano* **2010**, *5*, 366−373.

(39) Zhu, G.; Wang, A. C.; Liu, Y.; Zhou, Y.; Wang, Z. L. *Nano Lett.* **2012**, *12*, 3086−3090.

(40) Li, Z.; Zhu, G.; Yang, R.; Wang, A. C.; Wang, Z. L. *Adv. Mater.* **2010**, *22*, 2534−2537.

(41) Lee, S.; Hinchet, R.; Lee, Y.; Yang, Y.; Lin, Z.-H.; Ardila, G.; Montès, L.; Mouis, M.; Wang, Z. L. *Adv. Funct. Mater.* **2014**, *24*, 1163−1168.

(42) Gallo, L.; Placitelli, A. P.; Ciampi, M. Controller-Free Exploration of Medical Image Data: Experiencing the Kinect. In *24th International Symposium on Computer-Based Medical Systems (CBMS)*, 27−30 June 2011; IEEE: New York, 2011; pp 1−6.

(43) Burger, B.; Ferrané, I.; Lerasle, F.; Infantes, G. *Auton. Robot.* **2012**, *32*, 129−147.

(44) Xu, Z.; Xiang, C.; Yun, L.; Lantz, V.; Kongqiao, W.; Jihai, Y. *IEEE Trans. Syst., Man Cybern.* **2011**, *41*, 1064−1076.

(45) Fukui, R.; Watanabe, M.; Shimosaka, M.; Sato, T. *Int. J. Robot. Res.* **2014**, *33*, 658−671.

(46) Jeong, J. W.; Yeo, W. H.; Akhtar, A.; Norton, J. J. S.; Kwack, Y. J.; Li, S.; Jung, S. Y.; Su, Y. W.; Lee, W.; Xia, J.; Cheng, H. Y.; Huang, Y. G.; Choi, W. S.; Bretl, T.; Rogers, J. A. *Adv. Mater.* **2013**, *25*, 6839−6846.

(47) Ecoflex Series Technical Bulletin. http://www.smooth-on.com/tb/files/ECOFLEX_SERIES_TB.pdf (accessed Aug 25, 2014).

(48) Drake, R.; Vogl, A. W.; Mitchell, A. W. M. *Gray's Anatomy for Students*; Elsevier Health Sciences: New York, 2009.